ELSEVIER

Contents lists available at ScienceDirect

Biosensors and Bioelectronics

journal homepage: www.elsevier.com/locate/bios



A general design of pyridinium-based fluorescent probes for enhancing two-photon microscopy

Rui Chen ^a, Kangqiang Qiu ^b, Daniel C.Y. Leong ^a, Bidyut Kumar Kundu ^a, Chengying Zhang ^b, Prasenjit Srivastava ^c, Katie E. White ^c, Guodong Li ^a, Guanqun Han ^a, Ziyuan Guo ^d, Christopher G. Elles ^{c, **}, Jiajie Diao ^{b, ***}, Yujie Sun ^{a, *}

- ^a Department of Chemistry, University of Cincinnati, Cincinnati, OH 45221, USA
- ^b Department of Cancer Biology, College of Medicine, University of Cincinnati, Cincinnati, OH 45267, USA
- ^c Department of Chemistry, University of Kansas, Lawrence, KS 66045, USA
- ^d Cincinnati Children's Hospital Medical Center, Cincinnati, OH 45229, USA

ARTICLEINFO

Keywords: Two-photon bioimaging Mitochondria probe Lysosomes probe Organoids Super-resolution imaging

ABSTRACT

Two-photon absorbing fluorescent probes have emerged as powerful imaging tools for subcellular-level monitoring of biological substances and processes, offering advantages such as deep light penetration, minimal photodamage, low autofluorescence, and high spatial resolution. However, existing two-photon absorbing probes still face several limitations, such as small two-photon absorption cross-section, poor water solubility, low membrane permeability, and potentially high toxicity. Herein, we report three small-molecule probes, namely MSP-1arm, Lyso-2arm, and Mito-3arm, composed of a pyridinium center (electron-acceptor) and various methoxystyrene "arms" (electron-donor). These probes exhibit excellent fluorescence quantum yield and decent aqueous solubility. Leveraging the inherent intramolecular charge transfer and excitonic coupling effect, these complexes demonstrate excellent two-photon absorption in the near-infrared region. Notably, Lyso-2arm and Mito-3arm exhibit distinct targeting abilities for lysosomes and mitochondria, respectively. In two-photon microscopy experiments, Mito-3arm outperforms a commercial two-photon absorbing dye in 2D monolayer HeLa cells, delivering enhanced resolution, broader NIR light excitation window, and higher signal-to-noise ratio. Moreover, the two-photon bioimaging of 3D human forebrain organoids confirms the successful deep tissue imaging capabilities of both Lyso-2arm and Mito-3arm. Overall, this work presents a rational design strategy in developing competent two-photon-absorbing probes by varying the number of conjugated "arms" for bioimaging applications.

1. Introduction

In recent years, small-molecule fluorescent probes have emerged as essential and versatile tools for the real-time observation of biological processes (Grimm and Lavis, 2022; Kim and Cho, 2015; Wu et al., 2021; Yin et al., 2021). These probes possess the ability to freely enter cells and can be readily modified to target various biological substances, making them highly suitable for bioimaging requirements. Notably, advancements in chemical design strategies have paved the way for the creation of novel fluorophores with diverse properties. Currently, the majority of fluorescent probes employed for live cell imaging are based on

derivatives such as coumarin, anthracene, BODIPY, fluorescein, naphthalene amide, quinoline, and rhodamine (Beija et al., 2009; Boens et al., 2012; Cao et al., 2019; Chan et al., 2012; Duke et al., 2010). However, these fluorophores primarily operate through one-photon absorption, necessitating UV/visible light excitation. Unfortunately, this approach has several limitations. Firstly, the requirement for short-wavelength light excitation hinders deep tissue imaging due to poor penetration into media. Moreover, high-energy photons can induce photodamage to biological species. Additionally, many dyes exhibit low resistance to photobleaching, rendering them unsuitable for prolonged observation. Lastly, short-wavelength light can induce autofluorescence, which may

E-mail addresses: elles@ku.edu (C.G. Elles), jiajie.diao@uc.edu (J. Diao), yujie.sun@uc.edu (Y. Sun).

^{*} Corresponding author.

^{**} Corresponding author.

^{***} Corresponding author.

interfere with the original fluorescence signal (Wu et al., 2021).

In contrast, near-infrared (NIR) light excitation offers a solution to overcome the aforementioned limitations. Consequently, NIR fluorescent probes have attracted growing attention in the field of bioimaging (Chai et al., 2022; Yuan et al., 2013). NIR probes exhibit outstanding properties, including deep light penetration, low fluorescence background, high sensitivity, reduced photodamage, minimal autofluorescence, and non-invasiveness, providing scientists with many opportunities for in vivo imaging to explore and understand biological processes at the subcellular level (Guo et al., 2014; Yuan et al., 2013). Within this context, two-photon-absorbing fluorescent fluorophores have emerged as promising NIR probes that generate fluorescence signals through the simultaneous absorption of two photons, with each photon having a wavelength twice that of its corresponding one-photon absorption wavelength (Fig. S1a). Compared to one-photon imaging, two-photon imaging offers significantly higher spatial resolution as it occurs exclusively at the focal point of the pulsed laser beam (Bolze et al., 2017; Xu et al., 2020). However, most fluorophores employed in two-photon microscopy are originally designed for one-photon excitation and possess low two-photon absorption cross-sections (δ , 1 GM = 10⁻⁵⁰ cm⁴ s photon⁻¹ molecule⁻¹), limiting their applicability in two-photon microscopy (Makarov et al., 2008; Xu et al., 1996). Therefore, there is an urgent need to develop a diverse range of two-photon absorbing probes with exceptional performance, precise targeting capability, and excellent two-photon absorption cross-section in order to achieve enhanced two-photon microscopy.

Extensive research aimed at understanding the relationship between molecular structure and two-photon absorption has facilitated the rational design of two-photon absorbing fluorophores. Previous investigations have demonstrated that an increased degree of intramolecular charge transfer can result in a larger two-photon absorption cross-section (Kim and Cho, 2015; Wu et al., 2021). As depicted in Fig. S1b, there are general structural features that exhibit enhanced two-photon absorption: (1) Dipolar structure (D- π -A): This design incorporates an electron-donating group and an electron-accepting group connected through π -conjugation bridges, resulting in large transition dipole moment (Singh et al., 2022). (2) Quadrupolar structures ("pull-pull" $A-\pi$ -D- π -A or "push-push" $D-\pi$ -A- π -D): These structures involve extending the π -delocalized conjugation or increasing the symmetrical charge transfer from the middle of the molecule to the ends, or vice versa (Albota et al., 1998). (3) Octupolar structures (D $(-\pi$ -A)₃ or A $(-\pi-D)_3$): By introducing electron-donating or electron-accepting substituents with three dipolar branches, the two-photon absorption cross-section can be cooperatively amplified through excitonic coupling effects, which refer to the electronic coupling between the branches (Chung et al., 1999; Pascal et al., 2021; Singh et al., 2022; Terenziani et al., 2008). Although these design strategies have led to the development of many two-photon absorbing molecules with decent cross-sections, they often feature large planar conjugated backbones and hence poor solubility in aqueous media, limiting their applications in bioimaging (Hu et al., 2017; Macoas et al., 2011; Rodrigues et al., 2018). Besides, an increase in intramolecular charge transfer is often accompanied by a decrease in fluorescence, leading to a lower two-photon absorption "action" cross-section ($\delta\Phi$), a parameter dictating the bioimaging capability of a fluorescent probe (Kim and Cho, 2015; Wu et al., 2021). In recent years, there has been significant interest in developing two-photon-absorbing probes by replacing the acceptor in A (-π-D)₃ octupolar structures with metal cations, forming transition metal complexes coordinated with extended π -conjugation ligands, albeit with cytotoxicity concerns (Han et al., 2022; Karges et al., 2020; Wu et al., 2019).

To overcome these limitations, we embarked on exploring the potential of metal-free small organic molecules with multiple branches of π -delocalized conjugation for two-photon bioimaging. In this study, we present a rational design of a novel series of fluorophores featuring a pyridinium center moiety (electron acceptor) and 4-methoxystyrene

"arms" (electron donor). By incorporating the cationic charge, the methylpyridinium group exhibits enhanced electronegativity, improved aqueous solubility, and reduced π - π stacking. As a result, we observed red-shifts in both absorption and emission spectra, accompanied by amplification of two-photon absorption as the number of "arm" increases. Furthermore, the inclusion of a viscosity-sensitive vinylene group in these probes enhances the emission intensity under highviscosity conditions, thereby providing high signal-to-noise ratio for bioimaging. Through one-photon structured illumination microscopy (SIM), a super-resolution imaging technique, we observed distinct targeting abilities of the arm-system probes towards lysosomes and mitochondria. In comparison to commercially available two-photon absorbing dyes, our arm-system probes demonstrate superior twophoton imaging capabilities, including higher resolution, broader twophoton NIR light excitation window, and improved signal-to-noise ratio. Remarkably, our arm-system probes achieved excellent twophoton microscopy results of 3D human forebrain organoids, indicating their potential for deep-tissue bioimaging applications.

2. Results and discussion

2.1. Synthesis and photophysical properties of "arm" probes

As shown in Fig. 1a, depending on the number of "arms", we named three probes as MSP-1arm, Lyso-2arm, and Mito-3arm. The synthesis of MSP-1arm first started from the methylation of commercially available 4-methylpyridine (1) using methyl triflate, which resulted in 1,4-dimethylpyridinium (2). Next, condensation between 2 and 4-methoxybenzaldehyde produced the dipolar MSP-1arm with a yield of 76%. Analogously, the quadrupolar Lyso-2arm and octupolar Mito-3arm could be obtained via simply replacing 1 with commercially available 2,6-dimethylpyridine and 2,4,6-trimethylpyridine, respectively. The experimental details and characterization results of synthetic intermediates and final products are included in the supplementary information (Figs. S2–S7).

MSP-1arm exhibits prominent absorption in the near UV region with a peak at 372 nm ($\varepsilon=37,810~{\rm M}^{-1}{\rm cm}^{-1}$). Along with the increase of "arm" groups, bathochromic shifts are observed for the absorption spectra of Lyso-2arm and Mito-3arm, whose absorption maxima red shift to 387 nm ($\varepsilon=44,410~{\rm M}^{-1}{\rm cm}^{-1}$) and 396 nm ($\varepsilon=44,080~{\rm M}^{-1}{\rm cm}^{-1}$), respectively, with broad absorption tails beyond 450 nm (Fig. 1b). All of the three "arm" probes are highly fluorescent. Similar to the trend in the absorption spectra, their emission spectra also exhibit red shifts along with the increased number of "arm" groups. The fluorescence maximum of MSP-1arm is located at 493 nm, however, the emission peaks of Lyso-2arm and Mito-3arm move to 516 and 540 nm, respectively (Fig. 1c). Furthermore, the fluorescence quantum yields also increase from 1.3% for MSP-1arm to 2.7% for Lyso-2arm and 7.3% for Mito-3arm. These results strongly suggest that changing the "arm" numbers can largely modulate the photophysical properties of the resulting "arm" probes.

To detect the early processes of these fluorescent probes upon excitation, femtosecond transient absorption spectra were also collected with an excitation wavelength of 400 nm. As shown in Fig. 1d, the ground-state bleaching of Mito-3arm was observed between 380 and 420 nm. A prominent excited-state absorption band was detected in the range of 420–530 nm, which could be attributed to those intramolecular charge transfer states. Fitting the signals at 460 nm resulted in fast internal conversion and a longer excited-state lifetime, in agreement with the measurement of its emission lifetime (0.6 ns). The slight spectral shift could be due to the fast structural reorganization, including solvation dynamics, upon excitation. A similar pattern of transient absorption evolution could be observed for MSP-1arm and Lyso-2arm (Fig. S8), although the excited-state absorption peaks blue shifted and their lifetimes were shorter, 36 ps for MSP-1arm and 175 ps for Lyso-2arm.

To shed light on the above photophysical properties, density

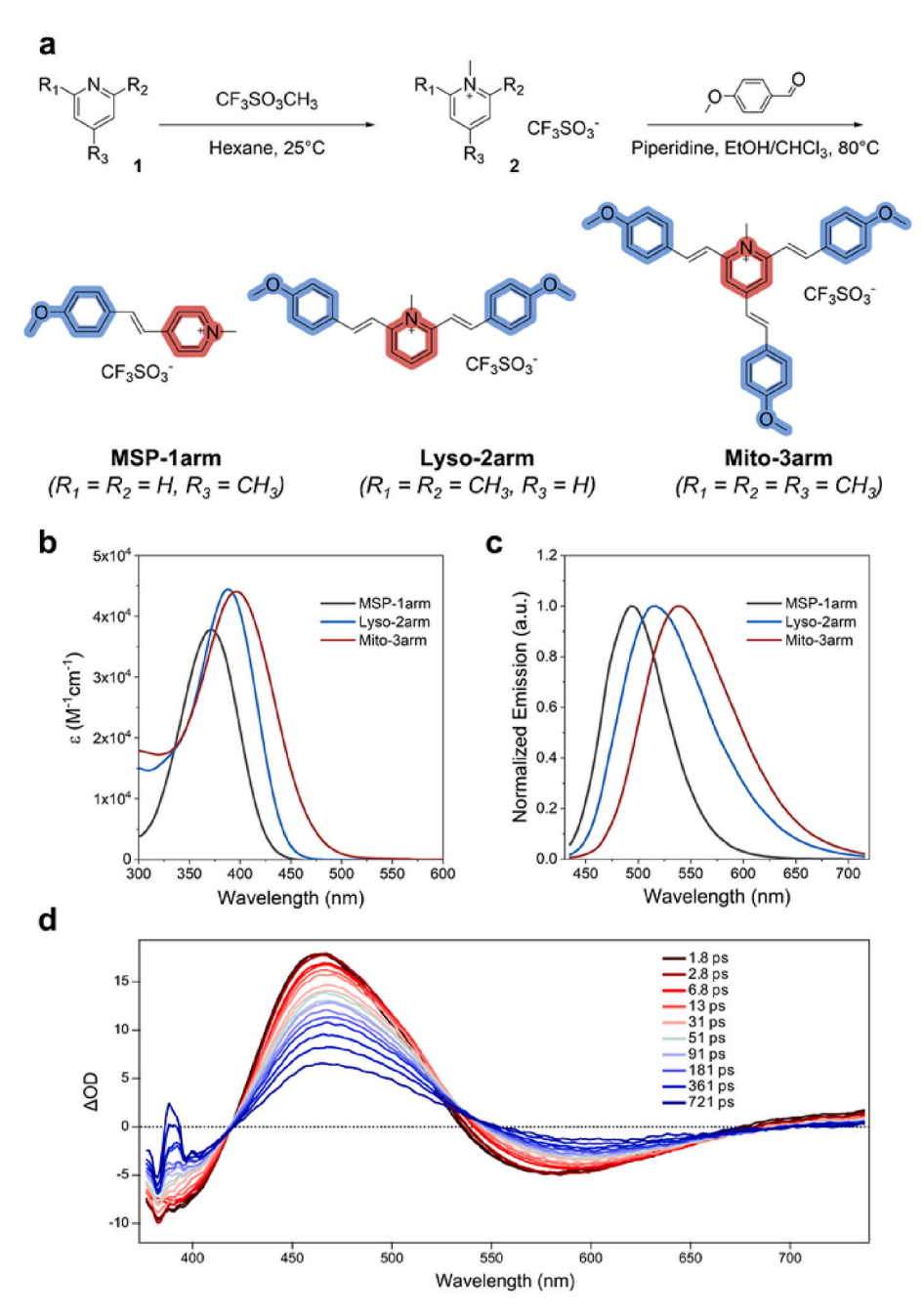


Fig. 1. (a) Synthetic scheme of MSP-1arm, Lyso-2arm, and Mito-3arm. (b) Absorption spectra of MSP-1arm, Lyso-2arm, and Mito-3arm in water. (c) Normalized emission spectra of MSP-1arm, Lyso-2arm, and Mito-3arm in water ($\lambda_{ex} = 405$ nm). (d) Transient absorption spectral evolution of Mito-3arm within 1 ns.

functional theory (DFT) calculations were also performed (Tables S1–S6). Fig. 2a presents the distribution of the highest occupied and lowest unoccupied molecular orbitals (HOMO/LUMOs) of these probes. All the HOMOs are primarily located at the peripheral methoxyphenyl ends, in agreement with their electron-donating capabilities. In contrast, the LUMOs are mainly distributed over the central pyridinium core, consistent with their positive charge and electron-deficient nature. In addition, along with the increase in "arm" groups, the HOMO-LUMO gap decreases from MSP-1arm (3.2 eV) to Lyso-2arm (3.08 eV) and Mito-3arm (2.95 eV). As expected, the time-dependent DFT calculation results indicate that the lowest singlet excited states (S1, mainly HOMO-LUMO transitions) show a red shift from MSP-1arm (377 nm) to Lyso-2arm (403 nm) and Mito-3arm (406 nm), matching their corresponding experimental absorption spectra quite well (Fig. 2b). Furthermore, the calculated electron density difference maps

(EDDMs) of S_1 states highlight the intra-molecular charge transfer character from the peripheral end(s) to the center upon excitation (Fig. 2c).

2.2. Viscosity-dependent emission

Since viscosity is not evenly distributed among subcellular organelles and the change in viscosity is closely related to many physiological and pathological processes (Dou et al., 2020; Kao et al., 1993), viscosity-dependent fluorescent probes have attracted increasing attention recently (Chai et al., 2022; Liang et al., 2021). It is known that the average viscosity is predominantly 2–4 cP (1 cP = 1 mPa·s) in cytoplasm, ~62 cP in mitochondrion, and ~65 cP in lysosome (Dijksterhuis et al., 2007; Wang et al., 2013; Yang et al., 2013). Hence, this drastic viscosity difference can be exploited to achieve better imaging

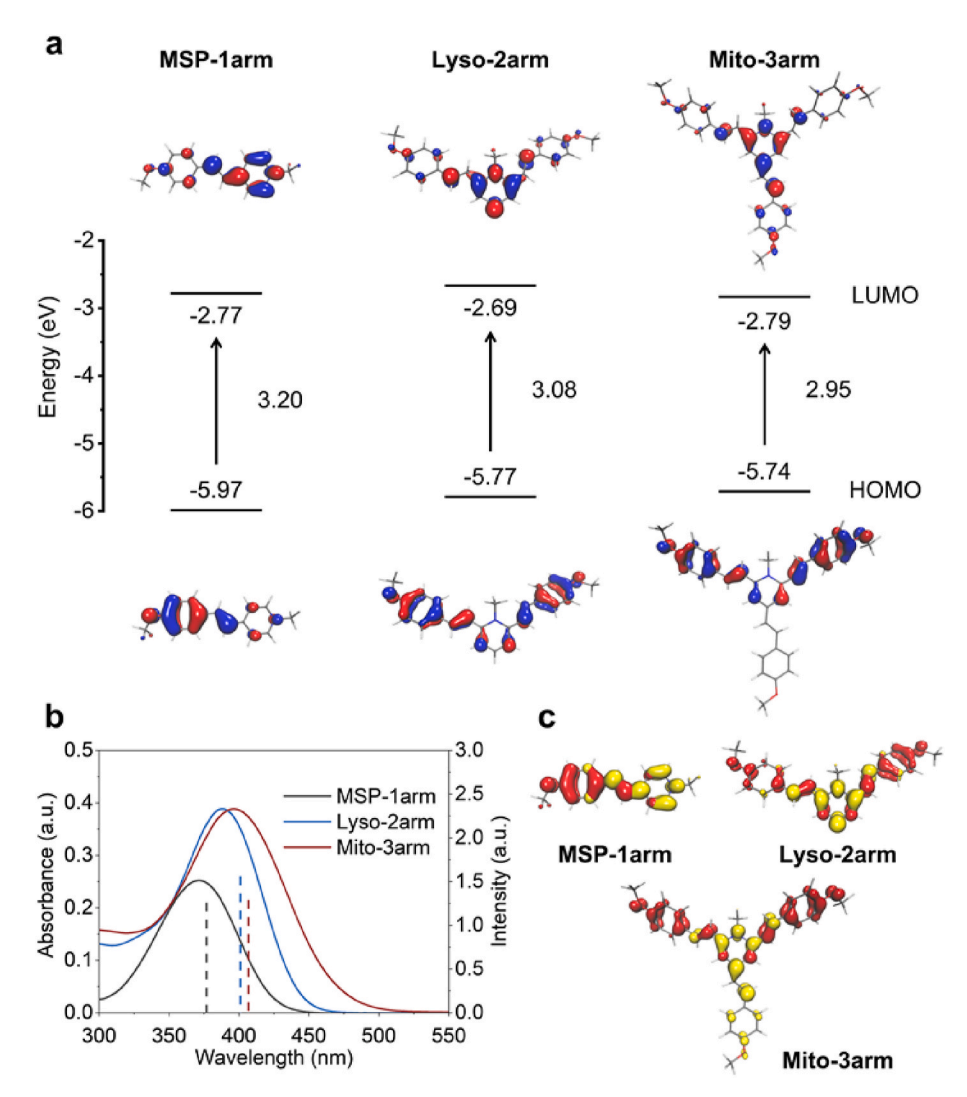


Fig. 2. (a) Calculated HOMOs and LUMOs of MSP-1arm, Lyso-2arm, and Mito-3arm. (b) Comparing the calculated wavelengths of the S₁ states with the experimental absorption spectra. (c) EDDMs of the S₁ states (red and yellow indicate decrease and increase in electron density, respectively).

results such as high signal-to-noise ratio (Chai et al., 2022; Chen et al., 2020a). Because of the presence of vinylene bridges in our "arm" probes, we suspected that the molecular rotation around these C=C bonds may result in viscosity-sensitive fluorescence. As shown in Fig. 3a and S9, all the probes exhibited slight red shifts in their absorption spectra collected $\,$ in glycerol versus in water. As expected, strong enhancement in fluorescence was observed for the three probes along with the increase of glycerol in water/glycerol mixed solutions. For instance, Fig. 3b presents the rapid rise of the emission intensity of MSP-1arm in water upon the continuous addition of glycerol. A nearly linear relationship between solution viscosity and fluorescence intensity was confirmed by fitting the Förster-Hoffmann equation (Fig. 3b inset) (Chen et al., 2019; Song et al., 2021; Zhu et al., 2014). Overall, a 6-fold enhancement was observed for MSP-1arm's emission from water to glycerol. The ratio of the fluorescence intensity of each probe measured in glycerol versus in water is compared in Fig. 3c. Given the presence of more vinylene bridges in Lyso-2arm and Mito-3arm, their fluorescence enhancements were even larger, 18- and 23-fold, respectively (Figs. S10 and S11). In agreement with its emission enhancement, the lifetime of Mito-3arm also increased from 0.6 ns in water to 1.5 ns in glycerol (Fig. 3d).

To assess whether the observed fluorescence enhancement can also be triggered by other factors, such as polarity, pH, ions, and biologically relevant species, we further collected their emission spectra under various conditions. Fig. S12 compiled the corresponding emission

spectra of each probe in different solvents, including THF, CHCl₃, CH₂Cl₂, acetone, DMF, DMSO, acetonitrile, ethanol, methanol, glycerol, water; while Fig. S13 plotted the relationship between the emission intensity of each probe and the polarity of the testing solvent. It is apparent that no clear relationship was obtained and the emission enhancement could only be detected in glycerol for all three probes. In addition, no drastic fluorescence change was observed for these probes in aqueous solutions when the pH varied from 4 to 8 (Fig. S14). Furthermore, as illustrated in Fig. S15, the presence of representative cations (Na $^{+},~K^{+},~Zn^{2+},~Fe^{2+},~Fe^{3+},~Mg^{2+},~Ag^{+},~Ni^{2+}),$ anions (NO $_{3}^{-},$ SO₄²-, Ac⁻, HCO₃, HSO₃, SCN⁻, F⁻, Cl⁻, Br⁻, I⁻), and reactive oxygen/ sulfur species (H₂O₂, glutathione, homocysteine, cysteine) led to negligible fluorescence variation for MSP-1arm, Lyso-2arm, and Mito-3arm in aqueous solutions. Finally, the fluorescence intensity of each probe was not altered during 300 s continuous irradiation (Fig. S16). Collectively, these above results demonstrate that the fluorescence of these "arm" probes is highly viscosity sensitive and the observed emission enhancement is not due to other factors but viscosity increase. The great photostability further renders them excellent fluorescent probes for bioimaging studies.

2.3. One-photon SIM imaging in live cells

Encouraged by the outstanding photophysical properties of the

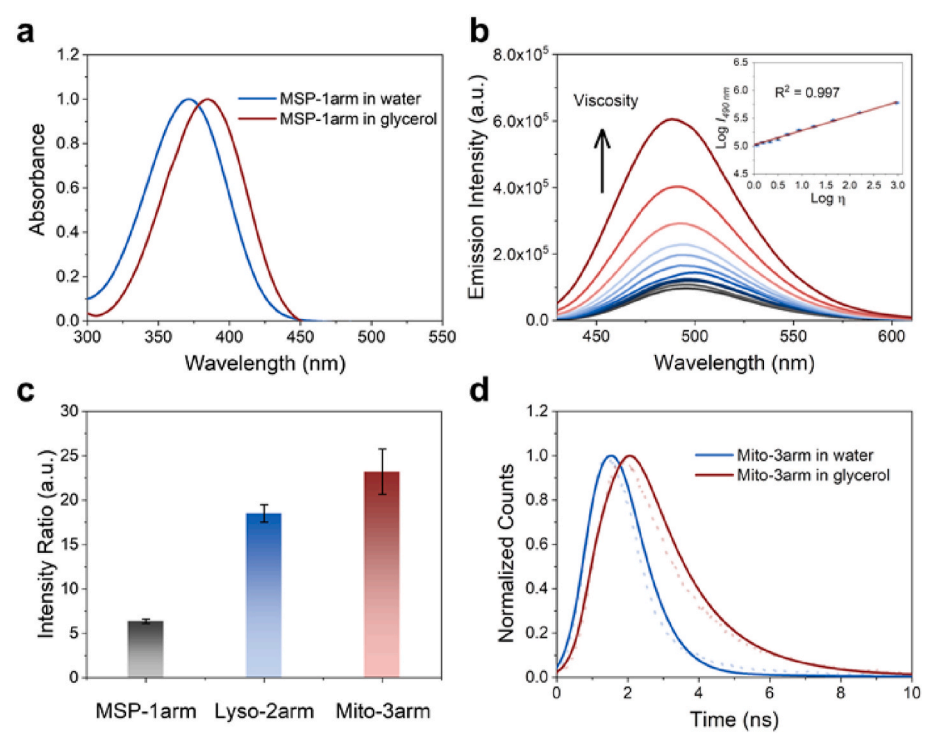


Fig. 3. (a) Absorption comparison of MSP-1arm in water versus in glycerol. (b) Emission spectra of MSP-1arm in water-glycerol mixed solution along with the increasing volume percentage of glycerol ($\lambda_{\rm ex}=371$ nm). Inset: the scatter plot and linear fitting between Log *I* (I: emission intensity at 490 nm) and Log η ($\eta=$ solution viscosity). (c) Emission intensity ratios of MSP-1arm, Lyso-2arm, and Mito-3arm in glycerol versus in water. (d) Emission decay profiles of Mito-3arm measured in water and glycerol.

above arm probes, we next investigated their potential applications in bioimaging using structured illumination microscopy (SIM) (Zhang et al., 2023). SIM is a novel technology that can overcome Abbe's diffraction limit in traditional confocal microscopy, providing better imaging results (Chen et al., 2020b, 2023; Fang et al., 2019, 2021; Qiu et al., 2022a, 2022b, 2022c; Wang et al., 2022). Since MSP-1arm has no absorption beyond 450 nm, shorter than the available excitation wavelength of our SIM instrument, hence we primarily used Lyso-2arm and Mito-3arm in the following studies. Based on the Cell Counting Kit-8 (CCK-8) assay, Lyso-2arm and Mito-3arm showed no significant decrease in cell viability after 24 h incubation with a concentration of 5 μM, suggesting that they can be employed in cellular experiments without toxicity concerns (Fig. S17). Taking Mito-3arm as an example, comparison of its fluorescence images collected via SIM versus conventional confocal microscopy clearly proved the better imaging quality and less background noise of the SIM images (Figs. \$18 and \$19).

Next, we co-stained these two probes with commercial lysosome dye LTR (LysoTracker Red) and mitochondrion dye MTDR (MitoTracker Deep Red) to find out their distribution in live cells. As shown in Fig. 4a and S20, Lyso-2arm and LTR exhibited the same puncta fluorescence and high overlap. The Pearson's correlation coefficient (PCC) value between Lyso-2arm and LTR was $\sim\!0.76$ (Fig. 4b). However, a much lower PCC value ($\sim\!0.18$) was measured between Lyso-2arm and MTDR (Fig. S21). On the other hand, Mito-3arm exhibited clear rod fluorescence (Fig. S22) with a high PCC value of $\sim\!0.77$ with MTDR (Fig. 4c and d) instead of LTR (Fig. S23). Overall, these SIM imaging results demonstrate that Lyso-2arm and Mito-3arm have distinct organelle targeting abilities towards lysosomes and mitochondria, respectively.

To understand the different targeting abilities of Lyso-2arm and Mito-3arm, we investigated their lipophilicity by measuring the *n*-octanol/water partition coefficient value (Log P). As illustrated in Fig. 4e and S24, along with the increase of "arm" groups, the Log P value increases from -0.3 for Lyso-2arm to 0.1 for Mito-3arm. Based on the theory of Horobin et al. a cation shows a high probability of lysosomal targeting when its Log P value is between -5 and 0, but prefers mitochondrial localization when the Log P value is between 0 and 5 (Horobin et al., 2013; Qiu et al., 2016). Therefore, the measured Log P values of

Lyso-2arm and Mito-3arm indicate that their different lipophilicity could be the primary reason for the distinct targeting abilities in live cells.

Next, we evaluated the photostability of Mito-3arm for long-term imaging studies. As shown in Fig. 4f–k, when exposed to continuous SIM laser at the 100% power mode, Mito-3arm displayed a much stronger photobleaching resistance than MTG. The fluorescence intensity of MTG disappeared quickly after 36 s laser exposure (Fig. 4h), however Mito-3arm retained 25% of its original fluorescence intensity even after 81 s laser irradiation (Fig. 4k).

2.4. Two-photon imaging in live cells

Along with an increase in the number of "arms", it was anticipated that two-photon absorption of our arm-type probes in the near infrared region would also be enhanced. Therefore, we collected the broadband two-photon absorption spectroscopy of all the probes using an ultrafast pump-probe technique (Figs. S25-S27). Fig. S27a compares the UV-vis absorption and the two-photon absorption spectra of Mito-3arm, plotted against the transition wavelength. Indeed, over 1200 GM of two-photon absorption could be obtained for Mito-3arm at the transition wavelength of 350 nm with a tail extended beyond 450 nm. In other words, it is feasible to collect two-photon microscopy of Mito-3arm using excitation light wavelength beyond 900 nm. Fig. S27b plotted the "action" crosssection ($\Phi\sigma_2$) profiles of MSP-1arm, Lyso-2arm, and Mito-3arm. Because Mito-3arm possesses the highest quantum yield and twophoton absorption cross-section, it is natural that it also shows the best action cross-section, followed by Lyso-2arm and then MSP-1arm. Therefore, the following two-photon microscopy studies were mainly performed using Mito-3arm as the fluorescent probe.

We then compared the one-photon microscopy (Fig. 5a, $\lambda_{\rm ex} = 488$ nm) and two-photon microscopy (Fig. 5f, $\lambda_{\rm ex} = 840$ nm) of Mito-3arm in the same emission window. By randomly zooming-in images captured by each microscopy (Fig. 5b,g), the cell morphology and boundaries between mitochondria and nucleus could be clearly identified in the two-photon microscopy. As expected, the FWHM of Mito-3arm image captured by two-photon microscopy was only 2.89 μ m (Fig. 5h), less

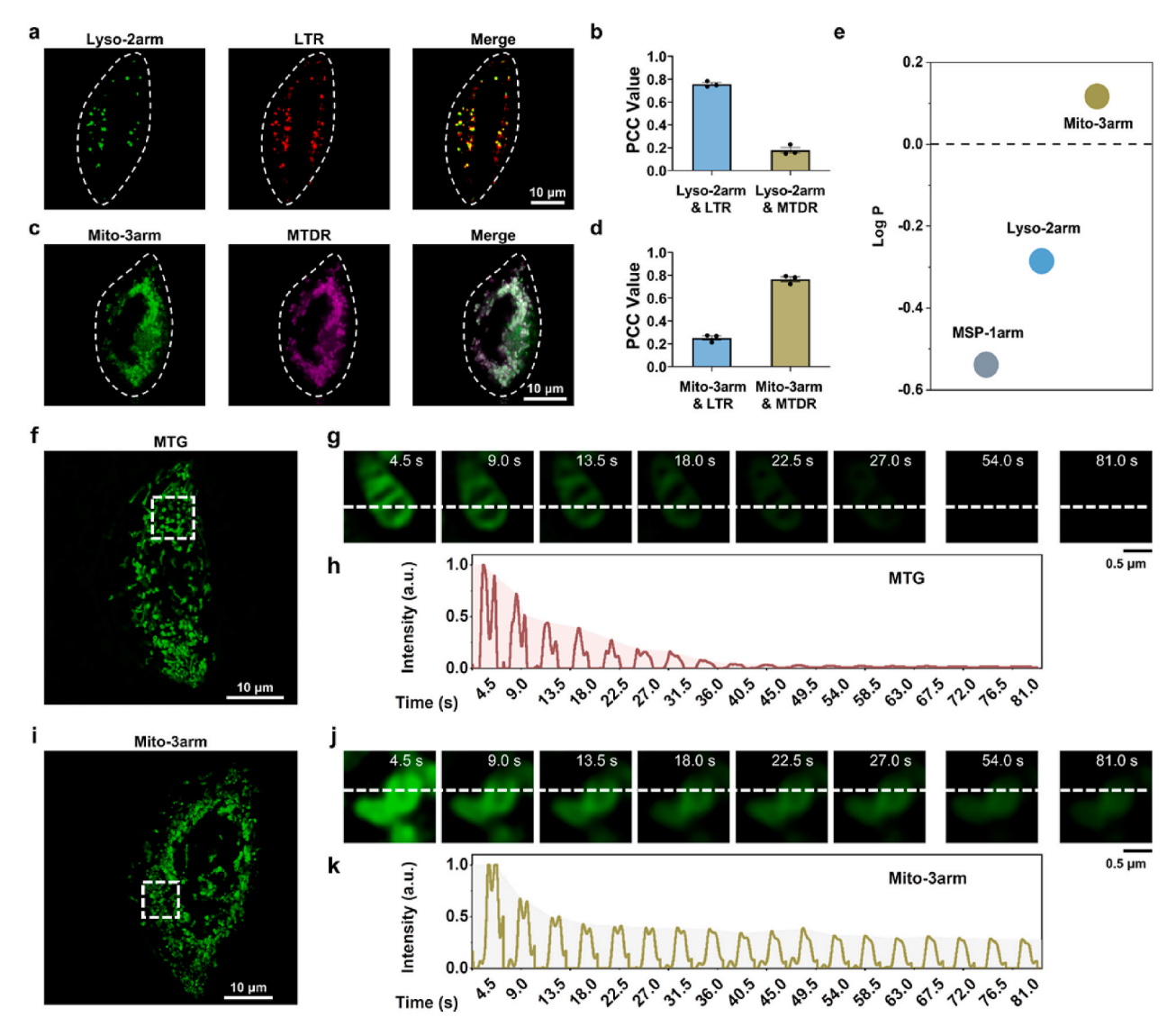


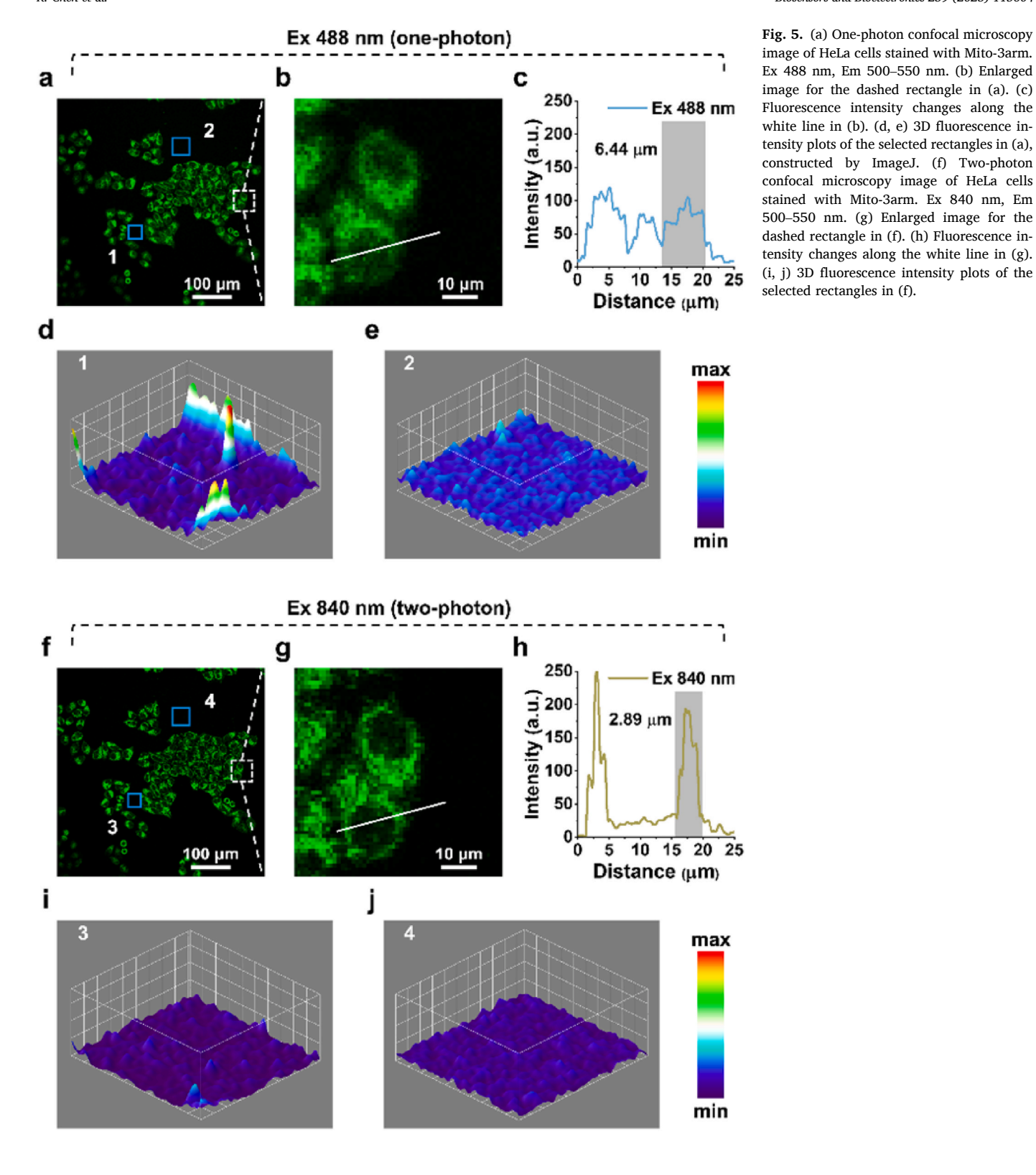
Fig. 4. (a) SIM images of HeLa cells co-stained with Lyso-2arm and LTR. (b) PCC values of Lyso-2arm with commercial dyes. (c) SIM images of HeLa cells co-stained with Mito-3arm and MTDR. (d) PCC values of Mito-3arm with commercial dyes. Data were presented as $M \pm SEM$ (n = 3). Lyso-2arm channel: Ex 488 nm, Em 500–550 nm; Mito-3arm channel: Ex 488 nm, Em 500–550 nm; LTR channel: Ex 561 nm, Em 570–640 nm; MTDR channel: Ex 640 nm, Em 660–735 nm. (e) Log P values of MSP-1arm, Lyso-2arm, and Mito-3arm. (f, g) Photobleaching property of MTG under continuous 488 nm laser irradiation at 100% power mode. (h) Normalized fluorescence intensity changes of MTG along the white dotted line in (g). (i, j) Photobleaching property of Mito-3arm under continuous 488 nm laser irradiation at 100% power mode. (k) Normalized fluorescence intensity changes of Mito-3arm along the white dotted line in (j).

than half of that measured by one-photon microscopy (6.44 µm, Fig. 5c).

Considering that Mito-3arm has a broad two-photon absorption profile in the near infrared region (i.e., transition wavelength ranges from 340 to 450 nm shown in Fig. S27a, hence a two-photon excitation window of 680-900 nm) and an emission peak around 540 nm, the excitation-induced background noise can be extremely reduced in upconversion fluorescence imaging. In addition, the autofluorescence emitted by intrinsic species such as flavins and NAD(P)H can be further vanished if using near infrared light as the excitation source, resulting in a high signal-to-noise ratio (Chatterjee et al., 2008; Georgakoudi et al., 2002; Monici, 2005). To demonstrate this merit, we stochastically selected two regions of background for both one-photon and two-photon images and drew their 3D fluorescence intensity distribution maps (Liu et al., 2020). The results strongly prove that the background fluorescence intensity of Mito-3arm in the two-photon excitation images (Fig. 5i and j) was significantly lower than that in the one-photon excitation images (Fig. 5d and e), in agreement with our hypothesis that the background noise of can be dramatically decreased in two-photon imaging under near infrared light excitation.

We next compared the two-photon bioimaging properties of Mito-3arm with a commercial two-photon absorbing mitochondrion dye MitoBlue (Sanchez et al., 2020). As expected, Mito-3arm and MitoBlue exhibited excellent co-localization with a PCC value of 0.84 (Fig. S28). Under three different two-photon excitation channels of 750, 840, and 900 nm, MitoBlue only showed appreciable fluorescence in the 750 nm channel due to its narrow two-photon absorption window. In contrast, Mito-3arm displayed bright and clear images in all channels (Fig. S29a). These observations are consistent with the calculated fluorescence intensity difference between MitoBlue and Mito-3arm in each channel (Figs. S29b–d), wherein comparable intensity was only measured in the 750 nm channel.

Subsequently, we compared the imaging contrast of MitoBlue and Mito-3arm, which is defined as the fluorescence intensity enhancement ratio of a dye to the background (Gong et al., 2016). As shown in Figs. S30a and b, we randomly selected four different regions of interest (ROI), where ROI1 represents the background (ROIB) and ROI2-4



represent the fluorescent dye (ROID). MitoBlue showed weak imaging brightness (Fig. S30c) and an ROID/ROIB ratio of 29-fold (Fig. S30e). Meanwhile, because of the viscosity-enhanced fluorescence, Mito-3arm not only displayed high imaging brightness (Fig. S30d) but also achieved a considerably high ROID/ROIB ratio of 82-fold. Furthermore, Mito-3arm displayed remarkable resistance to photobleaching in two-photon fluorescence imaging. As depicted in Fig. S31, under the excitation wavelength of 840 nm, Mito-3arm still exhibited distinct

fluorescence imaging and maintained high fluorescence intensity after 480 s continuous laser irradiation.

2.5. Two-photon imaging in organoids

Compared to two-dimensional (2D) cell models, 3D cultured organoids offer a more comprehensive representation of intercellular communication, as they encompass various cell types that engage in complex interactions. Organoids provide realistic human organ models for the study of relevant diseases, making them valuable for both basic research and clinical diagnosis and treatment (Koike et al., 2019; Lancaster and Knoblich, 2014; Shinozawa et al., 2016; Takebe and Wells James, 2019). Nevertheless, the increased depth of 3D organoids necessitates the use of longer wavelength light, preferably NIR photons, as the excitation source. Encouraged by the above two-photon microscopy results of Mito-3arm in cells, we sought to further perform the bioimaging of Mito-3arm in organoids. Specifically, the human forebrain organoids approximately ${\sim}600~\mu{\rm m}$ in size derived from human embryonic stem cells were treated with Mito-3arm.

To explore whether Mito-3arm can penetrate 3D organoids and achieve deep-tissue imaging, fluorescent images were captured at every 1.5 μm depth by using the Z-stack model of confocal microscopy in both one-photon (488 nm) and two-photon (840 nm) channels. As shown in Fig. 6a, the fluorescence of Mito-3arm was observed in organoids, which indicates that Mito-arm is able to break the matrix between cells in organoids and enable imaging of large tissue regions. While the one-photon fluorescence imaging revealed very faint fluorescent signals in organoids, the great two-photon action cross section of Mito-3arm in the NIR region resulted in bright and clear green fluorescence signals in nearly each depth layer of organoids. Tracking the central fluorescence intensity at different depths of organoids revealed that the one-photon imaging signal vanished at a depth of 120 μm (Fig. 6b). In contrast, its two-photon imaging was able to provide detectable signals even at a depth of 160 μm (Fig. 6c).

Finally, the Z-stack reconstruction images and 3D fluorescence intensity thermal maps of organoids obtained through one-photon and two-photon excitation are further compared. As shown in Fig. 6d, the one-photon 3D images only displayed weak fluorescence from the surface of organoids. However, the corresponding two-photon 3D images exhibited much stronger fluorescence from not only the surface but also the inner side of organoids (Fig. 6e). Increasing the incubation time of Mito-3arm could further enhanced the two-photon imaging of organoids (Fig. 6f and g). In addition, excellent two-photon imaging of Mito-3arm in 3D organoids could be obtained in excitation channels of 750 and 900 nm as well (Fig. S32), consistent with the results measured in 2D monolayer cells.

Besides Mito-3arm, Lyso-2arm was also employed in the two-photon imaging of organoids. As shown in Figs. S33–S35, Lyso-2arm indeed exhibited decent two-photon imaging properties under the excitation of 750, 840, and 900 nm, in agreement with its two-photon absorption profile (Fig. S26).

3. Conclusions

In summary, we have demonstrated that, built upon a pyridinium center, varying the number of π -conjugated methoxystyrene arms is an effective strategy in developing competent organic TPA fluorescent probes for bioimaging, thanks to the prominent intramolecular charge transfer and excitonic coupling effect between branches. Owing to their positive charge, these arm probes are soluble in aqueous media without

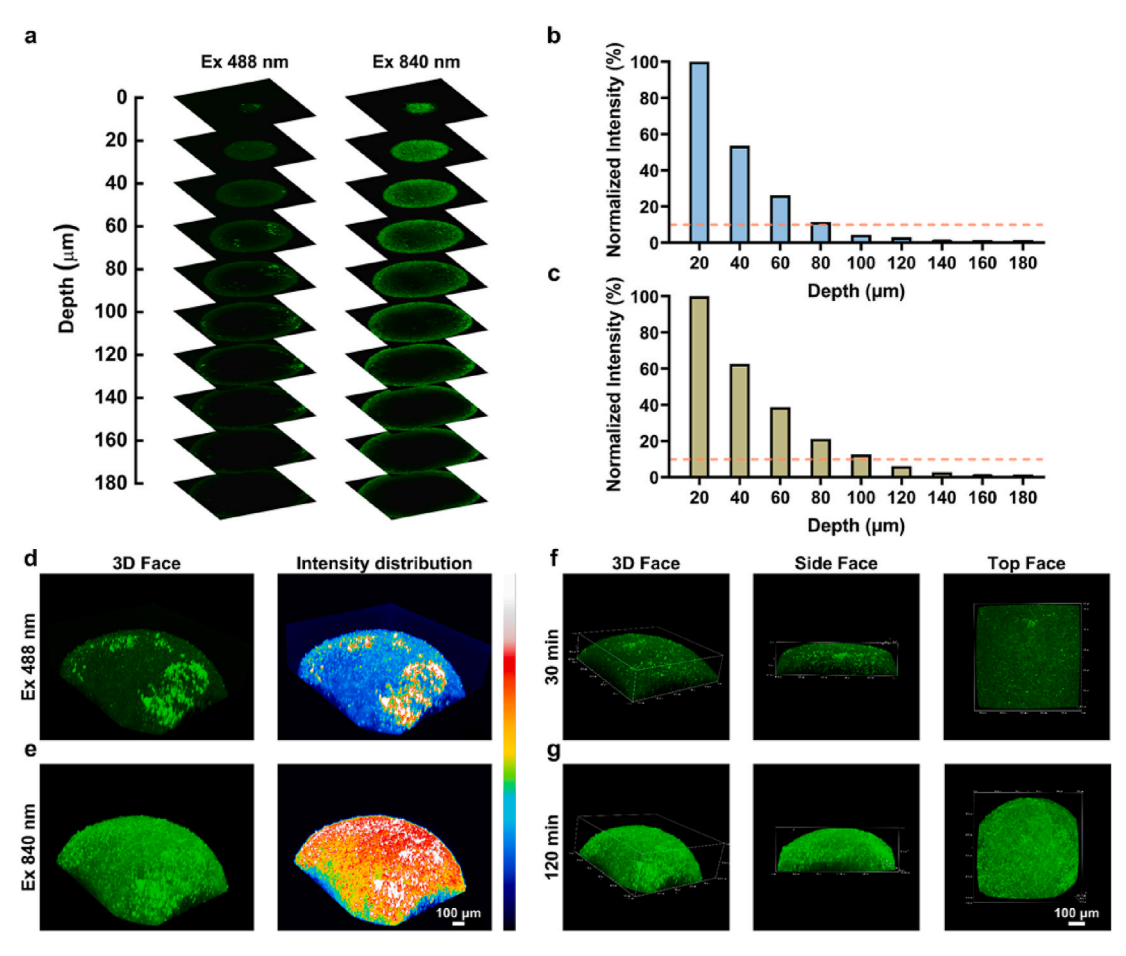


Fig. 6. (a) Z-stack confocal microscopy images of organoids stained with Mito-3arm were recorded at different imaging depths using one-photon (488 nm) or two-photon (840 nm) excitation. Central fluorescence intensity plots were generated for one-photon (b) or two-photon (c) excitation, showing the relationship with imaging depth. 3D reconstructions of Z-stack confocal microscopy images were created for organoids under (d) one-photon or (e) two-photon excitation, along with corresponding fluorescence intensity distribution maps, constructed by ImageJ. Two-photon confocal microscopy images of organoids stained with Mito-3arm were obtained at different time points: (f) 30 min and (g) 120 min.

 $\pi\text{-}\pi$ stacking. Variation in the number of "arms" also resulted in distinct lipophilicity of Lyso-2arm and Mito-3arm, rendering them with high targeting specificity towards lysosomes and mitochondria, respectively. In addition, the alkene-bridge arms also led to viscosity-sensitive fluorescence, beneficial for obtaining high signal-to-noise ratio in subcellular organelles. Notably, Mito-3arm exhibits great two-photon imaging capability for deep-tissue environments, including high resolution and wide NIR light excitation window, superior to the commercially purchased dye MitoBlue. These results highlight the promising potential of Mito-3arm for various bioimaging applications, especially in the observation of the dynamics of mitochondria.

In comparison to previously reported two-photon fluorescent probes featuring large π -conjugation structures (Table S7), our arm-system probes show distinct merits. First, the synthetic routes are straightforward, allowing facile production on a large scale. Second, Lyso-2arm and Mito-3arm exhibit symmetrical quadrupolar and octupolar configurations, respectively, resulting in significantly enhanced two-photon absorption cross-section values. Most notably, these "arm" probes have decent solubility in aqueous media and their targeting capability to different subcellular organelles can be precisely regulated by varying the number of "arms". These attributes highlight the promising prospects of our probes for advanced fluorescence imaging. Ongoing work centers on the development of new TPA fluorescent probes based on the core structure of these "arm" probes integrated with diverse functional moieties. In summary, the success of our arm-based probes opens an avenue in the rational design of molecular TPA fluorescent probes built upon small organic cations with diverse targeting specificities and enhanced TPA capability.

CRediT authorship contribution statement

Rui Chen: Investigation, Methodology, Data curation, Writing – original draft. Kangqiang Qiu: Methodology. Daniel C.Y. Leong: Methodology. Bidyut Kumar Kundu: Software. Chengying Zhang: Methodology. Prasenjit Srivastava: Methodology. Katie E. White: Methodology. Guodong Li: Methodology. Guanqun Han: Software. Ziyuan Guo: Methodology. Christopher G. Elles: Writing – review & editing, Funding acquisition, Jiajie Diao: Conceptualization, Writing – review & editing, Supervision, Funding acquisition. Yujie Sun: Conceptualization, Writing – review & editing, Supervision, Funding acquisition.

Declaration of competing interest

The authors declare that they have no known competing financial interests or personal relationships that could have appeared to influence the results and conclusions of this paper.

Data availability

Data will be made available on request.

Acknowledgements

Y.S. acknowledges the support of the National Science Foundation (CHE-1955358), University of Cincinnati, and the Ohio Supercomputer Center. J.D. thanks the National Institute of Health (R35GM128837). C. G.E. acknowledges support from the National Science Foundation (CHE-1905334). The confocal was supported by the NIH Shared Instrumentation Grant (S100D030402).

Appendix A. Supplementary data

Supplementary data to this article can be found online at https://doi.org/10.1016/j.bios.2023.115604.

References

Albota, M., Beljonne, D., Brédas, J.-L., Ehrlich, J.E., Fu, J.-Y., Heikal, A.A., Hess, S.E., Kogej, T., Levin, M.D., Marder, S.R., McCord-Maughon, D., Perry, J.W., Röckel, H., Rumi, M., Subramaniam, G., Webb, W.W., Wu, X.-L., Xu, C., 1998. Science 281, 1653–1656.

Beija, M., Afonso, C.A., Martinho, J.M., 2009. Chem. Soc. Rev. 38, 2410-2433.

Boens, N., Leen, V., Dehaen, W., 2012. Chem. Soc. Rev. 41, 1130-1172.

Bolze, F., Jenni, S., Sour, A., Heitz, V., 2017. Chem. Commun. 53, 12857–12877.
Cao, D., Liu, Z., Verwilst, P., Koo, S., Jangjili, P., Kim, J.S., Lin, W., 2019. Chem. Rev. 119, 10403–10519.

Chai, L., Liang, T., An, Q., Hu, W., Wang, Y., Wang, B., Su, S., Li, C., 2022. Anal. Chem. 94, 5797–5804.

Chan, J., Dodani, S.C., Chang, C.J., 2012, Nat. Chem. 4, 973-984.

Chatterjee, D.K., Rufaihah, A.J., Zhang, Y., 2008. Biomaterials 29, 937–943.

Chen, B., Li, C., Zhang, J., Kan, J., Jiang, T., Zhou, J., Ma, H., 2019. Chem. Commun. 55, 7410–7413.

Chen, Q., Fang, H., Shao, X., Tian, Z., Geng, S., Zhang, Y., Fan, H., Xiang, P., Zhang, J., Tian, X., Zhang, K., He, W., Guo, Z., Diao, J., 2020a. Nat. Commun. 11, 6290.

Chen, Q., Shao, X., Hao, M., Fang, H., Guan, R., Tian, Z., Li, M., Wang, C., Ji, L., Chao, H., Guan, J.-L., Diao, J., 2020b. Biomaterials 250, 120059.

Chen, R., Wang, L., Ding, G., Han, G., Qiu, K., Sun, Y., Diao, J., 2023. ACS Sens. 8, 2068–2078.

Chung, S.-J., Kim, K.-S., Lin, T.-C., He, G.S., Swiatkiewicz, J., Prasad, P.N., 1999. J. Phys. Chem. B 103, 10741–10745.

Dijksterhuis, J., Nijsse, J., Hoekstra, F.A., Golovina, E.A., 2007. Eukaryot. Cell 6, 157–170.

Dou, K., Huang, W., Xiang, Y., Li, S., Liu, Z., 2020. Anal. Chem. 92, 4177–4181. Duke, R.M., Veale, E.B., Pfeffer, F.M., Kruger, P.E., Gunnlaugsson, T., 2010. Chem. Soc. Rev. 30, 3936–3953

Fang, H., Geng, S., Hao, M., Chen, Q., Liu, M., Liu, C., Tian, Z., Wang, C., Takebe, T., Guan, J.-L., Chen, Y., Guo, Z., He, W., Diao, J., 2021. Nat. Commun. 12, 109.

Fang, H., Yao, S., Chen, Q., Liu, C., Cai, Y., Geng, S., Bai, Y., Tian, Z., Zacharias, A.L., Takebe, T., Chen, Y., Guo, Z., He, W., Diao, J., 2019. ACS Nano 13, 14426–14436.

Georgakoudi, I., Jacobson, B.C., Müller, M.G., Sheets, E.E., Badizadegan, K., Carr-Locke, D.L., Crum, C.P., Boone, C.W., Dasari, R.R., Van Dam, J., Feld, M.S., 2002. Cancer Res. 62, 682–687.

Gong, Y.J., Zhang, X.B., Mao, G.J., Su, L., Meng, H.M., Tan, W., Feng, S., Zhang, G., 2016.
Chem. Sci. 7, 2275–2285.

Grimm, J.B., Lavis, L.D., 2022. Nat. Methods 19, 149-158.

Guo, Z., Park, S., Yoon, J., Shin, I., 2014. Chem. Soc. Rev. 43, 16-29.

Han, G., Li, G., Huang, J., Han, C., Turro, C., Sun, Y., 2022. Nat. Commun. 13, 2288.Horobin, R.W., Rashid-Doubell, F., Pediani, J.D., Milligan, G., 2013. Biotech. Histochem. 88, 440–460.

Hu, L., Wang, H., Xu, X., Zhang, M., Tian, X., Wu, J., Zhou, H., Yang, J., Tian, Y., 2017. Sens. Actuators, B 241, 1082–1089.

Kao, H.P., Abney, J.R., Verkman, A.S., 1993. J. Cell Biol. 120, 175-184.

Karges, J., Kuang, S., Maschietto, F., Blacque, O., Ciofini, I., Chao, H., Gasser, G., 2020. Nat. Commun. 11, 3262.

 $\label{eq:Kim, H.M., Cho, B.R., 2015. Chem. Rev. 115, 5014–5055.}$

Koike, H., Iwasawa, K., Ouchi, R., Maezawa, M., Giesbrecht, K., Saiki, N., Ferguson, A., Kimura, M., Thompson, W.L., Wells, J.M., Zorn, A.M., Takebe, T., 2019. Nature 574, 112–116.

Lancaster, M.A., Knoblich, J.A., 2014. Science 345, 1247125.

Liang, T., Zhang, D., Hu, W., Tian, C., Zeng, L., Wu, T., Lei, D., Qiang, T., Yang, X., Sun, X., 2021. Talanta 235, 122719.

Liu, L.Y., Fang, H., Chen, Q., Chan, M.H., Ng, M., Wang, K.N., Liu, W., Tian, Z., Diao, J., Mao, Z.W., Yam, V.W., 2020. Angew. Chem., Int. Ed. Engl. 59, 19229–19236.

Macoas, E., Marcelo, G., Pinto, S., Caneque, T., Cuadro, A.M., Vaquero, J.J., Martinho, J. M., 2011. Chem. Commun. 47, 7374–7376.

Makarov, N.S., Drobizhev, M., Rebane, A., 2008. Opt Express 16, 4029-4047.

Monici, M., 2005. Cell and Tissue Autofluorescence Research and Diagnostic Applications. Biotechnol. Annu. Rev. Elsevier, pp. 227–256.

Pascal, S., David, S., Andraud, C., Maury, O., 2021. Chem. Soc. Rev. 50, 6613–6658.
 Qiu, K., Liu, Y., Huang, H., Liu, C., Zhu, H., Chen, Y., Ji, L., Chao, H., 2016. Dalton Trans.
 45. 16144–16147.

Qiu, K., Seino, R., Han, G., Ishiyama, M., Ueno, Y., Tian, Z., Sun, Y., Diao, J., 2022a. Adv. Healthcare Mater. 11, 2102185.

Qiu, K., Yadav, A., Tian, Z., Guo, Z., Shi, D., Nandi, C.K., Diao, J., 2022b. ACS Mater. Lett. 4, 1565–1573.

Qiu, K., Zou, W., Fang, H., Hao, M., Mehta, K., Tian, Z., Guan, J.L., Zhang, K., Huang, T., Diao, J., 2022c. Nat. Commun. 13, 4303.

Rodrigues, A.C.B., Mariz, I.d.F.A., Maçoas, E.M.S., Tonelli, R.R., Martinho, J.M.G., Quina, F.H., Bastos, E.L., 2018. Dyes Pigments 150, 105–111.

Sanchez, M.I., Vida, Y., Perez-Inestrosa, E., Mascarenas, J.L., Vazquez, M.E., Sugiura, A., Martinez-Costas, J., 2020. Sci. Rep. 10, 3528.

Shinozawa, T., Yoshikawa, H.Y., Takebe, T., 2016. Dev. Biol. 420, 221-229.

Singh, A.K., Nair, A.V., Singh, N.D.P., 2022. Anal. Chem. 94, 177–192.

Song, Y., Zhang, H., Wang, X., Geng, X., Sun, Y., Liu, J., Li, Z., 2021. Anal. Chem. 93, 1786–1791.

Takebe, T., Wells James, M., 2019. Science 364, 956-959.

Terenziani, F., Sissa, C., Painelli, A., 2008. J. Phys. Chem. B 112, 5079-5087.

Wang, L., Chen, R., Han, G., Liu, X., Huang, T., Diao, J., Sun, Y., 2022. Explorations 2, 20210215.

Wang, L., Xiao, Y., Tian, W., Deng, L., 2013. J. Am. Chem. Soc. 135, 2903–2906. Wu, L., Liu, J., Li, P., Tang, B., James, T.D., 2021. Chem. Soc. Rev. 50, 702–734.

- Wu, W., Guan, R., Liao, X., Yan, X., Rees, T.W., Ji, L., Chao, H., 2019. Anal. Chem. 91, 10266–10272.
- Xu, C., Zipfel, W., Shear, J.B., Williams, R.M., Webb, W.W., 1996. Proc. Natl. Acad. Sci. U.S.A. 93, 10763–10768.
- Xu, L., Zhang, J., Yin, L., Long, X., Zhang, W., Zhang, Q., 2020. J. Mater. Chem. C 8, 6342–6349.
- Yang, Z., He, Y., Lee, J.H., Park, N., Suh, M., Chae, W.S., Cao, J., Peng, X., Jung, H., Kang, C., Kim, J.S., 2013. J. Am. Chem. Soc. 135, 9181–9185.
- Yin, J., Huang, L., Wu, L., Li, J., James, T.D., Lin, W., 2021. Chem. Soc. Rev. 50, 12098–12150.
- Yuan, L., Lin, W., Zheng, K., He, L., Huang, W., 2013. Chem. Soc. Rev. 42, 622–661.
 Zhang, C., Tian, Z., Chen, R., Rowan, F., Qiu, K., Sun, Y., Guan, J.-L., Diao, J., 2023. Adv. Drug Deliv. Rev. 199, 114978.
- Zhu, H., Fan, J., Li, M., Cao, J., Wang, J., Peng, X., 2014. Chem. Eur J. 20, 4691-4696.